# In Situ Electrochemical Interfacial Manipulation Enabling Lithiophilic Li Metal Anode with Inorganic-Rich Solid Electrolyte Interphases for Stable Li Metal Batteries

*Subin Kim, Ki-Yeop Cho, JunHwa Kwon, Kiyeon Sim, KwangSup Eom,\* and Thomas F. Fuller*

Lithium-metal anodes (LMAs) are the ultimate choice for realizing high-energy-density batteries; however, its use is hindered by problematic Li growth in the form of dendrites. To alleviate dendritic Li growth, the preparation of LMAs with a lithiophilic current collector (CC) is effective; however, applying a lithiophilic CC to LMAs is still challenging due to the manufacturing complexity involved in the separate lithiophilic treatment and lithiation processes. Herein, a facile one-pot LMA fabrication method by utilizing thiourea (TU) as a precursor is proposed. A lithiophilic $Cu_2S$ layer is formed on Cu foam (CF) by the in situ electrochemical oxidation of TU ($Cu_xSCF$), and the lithiation of CC is performed via subsequent Li electrodeposition ($Li@Cu_xSCF$). The $Cu_2S$ on $Cu_xSCF$ can lead to uniform Li deposition by providing lithiophilic sites, and it is converted to form ionic-conductive $Li_2S$-rich solid electrolyte interphase layer. Resultantly, $Cu_xSCF$ significantly enhances the cycling performance of LMAs compared to CF. Specifically, a $LiFePO_4/Li@Cu_xSCF$ full-cell lithium-metal battery (LMB) with a low $n/p$ ratio (1.6) exhibits capacity retention of 95.6% at 0.5 C (220 cycles) and can maintain 85.0% of initial capacity (425 cycles, $n/p = 4$) at 2.0 C. LMBs with $LiNi_{0.6}Co_{0.2}Mn_{0.2}$ and $LiNi_{0.8}Co_{0.1}Mn_{0.1}$ also exhibit improved electrochemical performance.

## 1. Introduction

The increasing demand for high-energy-density batteries has triggered exploration of battery systems that are more advanced than conventional lithium (Li) ion batteries.[1–3] Among the various alternatives, a lithium-metal battery (LMB) is an ideal candidate to achieve high-energy density owing to the exceptional capacity (3860 mAh g$^{-1}$) and low working potential ($-3.04$ V vs standard hydrogen electrode potential, of the lithium-metal anode (LMA).[4–6] However, hostless Li metal undergoes infinite volume changes during cycling.[7,8] This leads to persistent cracking and reconstruction of the fragile solid electrolyte interphase (SEI) and the formation of electrically isolated Li covered by the SEI layer, forming so-called "dead Li".[9,10] These side reactions result in the accelerated consumption of electrolyte and depletion of active Li, which shortens the lifespan and lowers the Coulombic efficiency (CE) of LMBs.[11,12] Furthermore, nonuniform Li nucleation and subsequent deposition induces dendritic Li growth.[13,14] These filament-like Li dendrites can penetrate the separator and cause short-circuiting, raising substantial safety concerns.[15,16] These challenging issues associated with LMAs have hindered the practical application of LMBs; hence, some innovative strategies are needed to alleviate extreme volume changes in Li and suppress Li dendrite formation.

To date, tremendous efforts have been devoted to developing stable LMAs. These include electrolyte modification,[17–19] the construction of artificial solid electrolyte interphase films,[20,21] and the application of functional separators.[22,23] These strategies successfully enhance the interface stability of LMAs and suppress Li dendrite formation to some extent, but they have limited effects on alleviating volume changes and improving the dimensional stability of LMAs due to their hostless structure. In this context, the utilization of a porous 3D current collector (3D CC) for Li hosts has been widely investigated because it can reduce effective current density by providing a large surface area to mitigate Li dendritic growth and accommodate Li deposits to alleviate volumetric changes, which have great potential for practical applications due to their low cost and large Li deposition capacity derived from their large porous structures. However, the lithiophobic property of these bare 3D CCs results in heterogeneous Li deposition, and the SEI on the bare 3D CC has sluggish Li$^+$ conductivity and weak mechanical strength and hence cannot effectively mitigate Li dendritic growth.[24] In addition,

S. Kim, K.-Y. Cho, J. H. Kwon, K. Sim, K. S. Eom
School of Materials Science and Engineering
Gwangju Institute of Science and Technology (GIST)
123 Cheomdangwagi-ro, Buk-gu, Gwangju 61005, Korea
E-mail: keom@gist.ac.kr

K. S. Eom, T. F. Fuller
School of Chemical & Biomolecular Engineering
Georgia Institute of Technology
Atlanta, GA 30332, USA

severe side reactions occur between Li and the electrolyte during the repair of the fractured SEI layer since the 3D CCs have a large surface area and accelerate electrolyte decomposition, significantly shortening the lifetime of the battery. Thus, methods to simultaneously endow 3D CCs with good lithiophilicity and reinforce the SEI layer with excellent ionic conductivity and mechanical strength should be considered to achieve stable LMAs.

To date, various lithiophilic materials have been utilized for the surface modification of 3D CCs, such as Ag,[25] Au,[26] Zn,[27] and Sn,[28] to inhibit Li dendrite growth by inducing homogenous Li deposition. Such a lithiophilic metal layer on 3D CCs could homogenize Li$^+$ flux effectively and lead to uniform Li nucleation and deposition; however, it has a limited effect on stabilizing the SEI layer. In this context, the application of conversion-type materials, such as metallic oxides (CuO,[29] ZnO[30]), nitrides (M$_x$N[31]), and sulfides (Ni$_3$S$_2$,[32] Cu$_2$S[33,34]), as coating layers for 3D CCs has emerged as a promising approach. These conversion-type materials have good lithiophilicity owing to their high Li$^+$ affinity, and they can generate a stable SEI layer via conversion reactions. Specifically, a metal sulfide (MS$_x$) coating is highly effective for stabilizing LMAs owing to the lithiophilic behavior of MS$_x$ and for the formation of a Li$_2$S-rich SEI layer.[32–34] 1) Li$_2$S facilitates fast Li$^+$ transport and homogeneous Li growth with its high ionic conductivity ($\approx10^{-5}$ S cm$^{-1}$) and low Li$^+$ diffusion energy barrier.[21,35] 2) Li$_2$S mitigates electrolyte decomposition through its high mechanical strength and electrical insulating properties.[36,37]

In contrast, since lithium insertion (lithiation) must be performed to utilize the prepared CCs as a full-cell anode, this process is also considered important in the fabrication of LMAs. In general, the fabrication of LMA with surface-modified CC requires a two-step process, ex situ surface treatment of CC and further lithiation of CC. Since metallic Li is highly sensitive toward various chemicals, moisture, and oxygen, this two-step process of LMA fabrication introduces difficulties in handling and extra costs.[38–40] For instance, precursors such as NaOH or hydrazine hydrate employed for the surface treatment of

CC can have adverse effects on the subsequent lithiation process and battery operation, necessitating washing/drying processes prior to use.[33] Moreover, the ex situ surface treatment of CCs requires multiple procedural steps, the use of various toxic solutions, and considerable treatment time to obtain the final products. In this context, integrating the surface treatment of CC and lithiation into a one-pot process for the construction of LMAs could be an efficient method that can reduce time, cost, and the effect of detrimental conditions on LMB operation; however, studies on this method are limited.

Hence, we propose a facile one-pot method to fabricate highly stable LMA, by which the in situ formation of a lithiophilic Cu$_2$S layer and subsequent electroplating of Li (lithiation) can be conducted in one electrochemical cell. In particular, thiourea (TU) could be employed as an electrolyte additive as a precursor for Cu$_2$S, which is known as lithiophilic material. The reasons to employ TU as an additive are as follows: 1) TU can be electrochemically oxidized to form Cu$_2$S by reacting with Cu foam even at a low concentration[41,42] ($\sim$20 mM); and 2) TU is compatible with a conventional battery electrolyte system[43,44] (1 M LiTFSI in 1,3-dioxolane (DOL)/1,2-dimethoxyethane (DME) + LiNO$_3$); thus, Cu$_2$S formation and electroplating of Li can occur in the same electrolyte. In this work, the effects of TU on the oxidation behavior of Cu CCs and the corresponding formation of LMAs as determined by oxidation conditions (voltage hold) were extensively studied via surface-chemical/morphological and electrochemical analyses. Moreover, the optimized LMAs were used to construct full-cell lithium metal batteries using LiFePO$_4$, LiNi$_{0.6}$Co$_{0.2}$Mn$_{0.2}$ and LiNi$_{0.8}$Co$_{0.1}$Mn$_{0.1}$ cathodes and analyzed using various electrochemical performance tests to study feasibility.

## 2. Anodic Formation of Cu$_x$S on Cu Foam and One-Pot Fabrication of Li@Cu$_x$SCF

**Figure 1** illustrates our proposed electrochemical one-pot LMA fabrication method. By utilizing the oxidation reaction of TU,



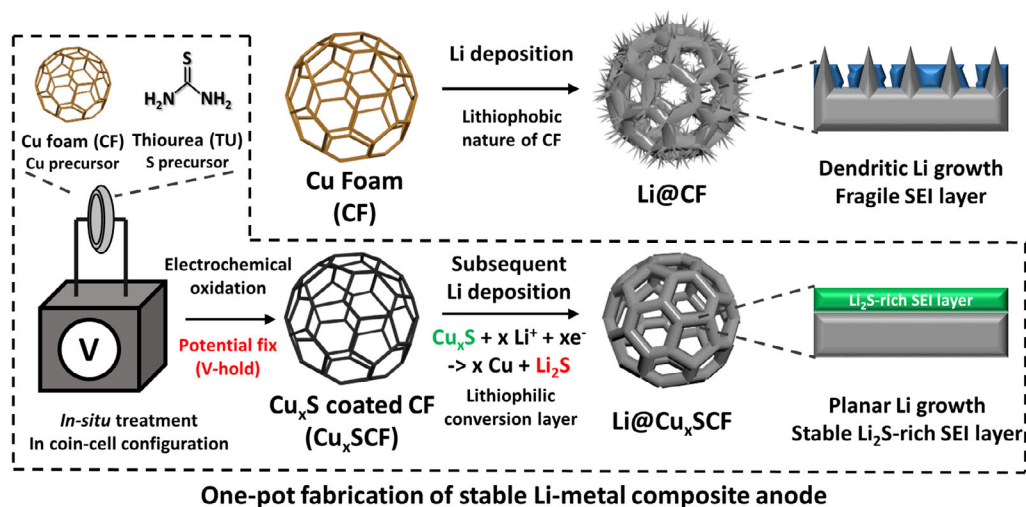**Figure 1.** Schematic of the electrochemical one-pot fabrication method of lithiophilic LMA (Li@Cu$_x$SCF) and Li deposition behavior on different current collectors.

ADVANCED
SCIENCE NEWS
www.advancedsciencenews.com

small
structures
www.small-structures.com

a $Cu_2S$ layer could be constructed directly on the Cu foam (denoted as $Cu_xSCF$) in the Li/Cu cell by applying a constant oxidation potential (V-hold). In addition, subsequent electrodeposition of Li is also possible in the same electrolyte; thus, one-pot fabrication of a Li composite anode along with surface treatment (Li@$Cu_xSCF$) is possible through an electrochemical method. Note that the $Cu_2S$ layer can provide lithiophilic sites due to its good $Li^+$ affinity, leading to homogeneous Li deposition. Moreover, $Cu_2S$ can be converted into $Li_2S$ and Cu, as shown in Equation (1).[33]

$$Cu_2S + 2Li^+ + 2e^- \rightarrow 2Cu + Li_2S \qquad (1)$$
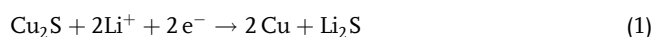
The conversion reaction of $Cu_2S$ leads to the formation of a $Li_2S$-rich SEI layer, enabling smooth and dendrite-free lithium growth due to the good ionic conductivity and mechanical strength of $Li_2S$. Thus, $Cu_xSCF$ can effectively suppress Li dendrite growth, enabling stable Li cycling. Hence, we could expect that this one-pot fabricated LMA, Li@$Cu_xSCF$ can serve as a stable LMA to improve the cycling performance of LMBs, in contrast to Li@CF in which severe Li dendrite growth is induced by a lithiophobic CC surface and a weak naturally formed SEI layer.

To verify our suggested method, we investigated the oxidation reactions occurring on the Cu electrode in the presence of TU. As shown in the linear sweep voltammetry (LSV) curve (**Figure 2**a), the Li/Cu cell without the TU additive does not show an apparent peak other than the Cu dissolution peak denoted as $E_{1a}$ at ≈3.4 V. However, the Li/Cu cell with the TU additive shows several anodic peaks labeled $E_{1b}$, $E_{2b}$, and $E_{3b}$, which appear at 2.1, 2.6, and 2.9 V, respectively. According to a previous study, the oxidation reaction of TU on the Cu electrode could occur in sequential steps: 1) formation of a soluble film composed of the Cu(I)–TU complex (film 1) along with mild $Cu^{2+}$ dissolution; 2) oxidation of film 1 and TU into an insoluble film (film 2) consisting of S and $Cu_xS$; and 3) severe dissolution of the Cu electrode.[41,42] From the CV curves obtained from the Cu electrode and stainless steel (SS) electrode with electrolyte with and without TU (Figure 2b), we could observe negligible oxidation peaks on the SS electrode in contrast to the Cu electrode (shown as inset arrows in Figure 2b). This confirms that the investigated oxidation reactions shown in Figure 2a are indeed Cu-involved reactions with TU. Thus, it can be inferred that the formation of soluble TU–Cu complexes along with $Cu^{2+}$ dissolution ($E_{b1}$, 2.1 V), formation of S–Cu–$Cu_xS$ films ($E_{b2}$, 2.6 V), and severe dissolution of Cu electrodes ($E_{b3}$, 2.9 V) occurs sequentially during LSV measurements. In addition, the reduction peaks appearing at ≈1.3 and 0.6 V in Figure 2b could be associated with the decomposition of LiTFSI and DME,[21] and the reduction current increases when TU is added to the electrolyte. This could be ascribed to the catalytic role of TU in the reduction of electrolyte components.[44]

Next, we conducted electrochemical surface treatment of Cu foam by using the oxidation reaction of TU. For oxidative surface treatment, we applied constant potential on Cu foam (denoted as "V-hold" in this study) to avoid unwanted side reactions such as severe dissolution of Cu foam. Based on the aforementioned assumption, we chose 2.6 V as a potential for the formation of



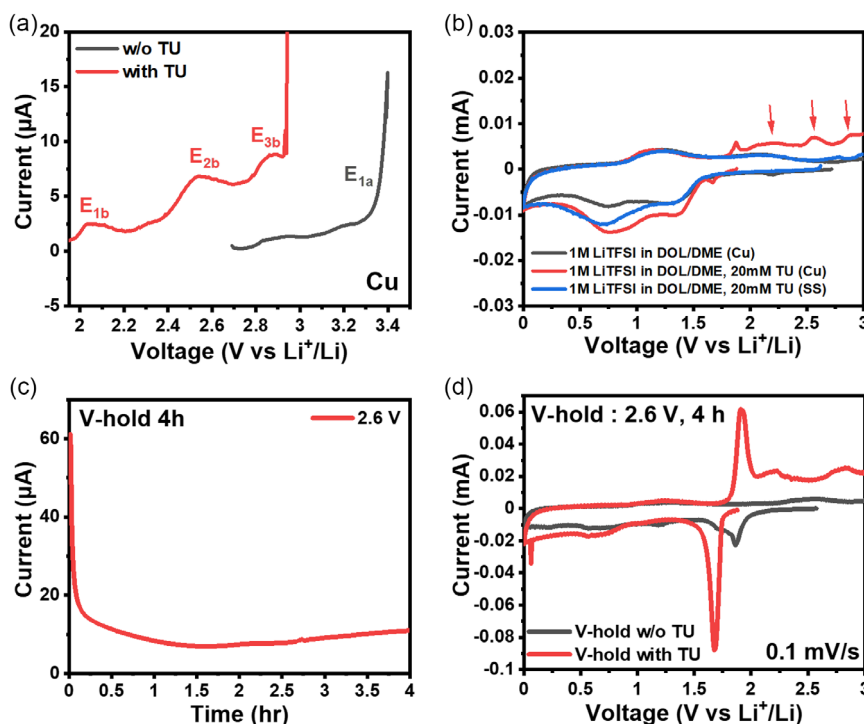**Figure 2.** a) LSV measurement on a Cu electrode with different electrolytes. b) Cyclic voltammetry (CV) curve in the Li/Cu cells with different electrolytes and electrodes (Cu and stainless steel (SS) electrodes). c) Time–current curve during V-hold at 2.6 V. d) Cyclic voltammetry (CV) curve in the base electrolyte in the Li/Cu cells after applying V-hold with different electrolytes (with TU and without TU).

$Cu_xS$ films on Cu foam without severe dissolution of Cu in this study. From the time–current curve measured during V-hold at 2.6 V in the presence of TU (Figure 2c), we could clearly observe the anodic reaction. When the anodic reaction starts, the oxidation current flows rapidly, which is due to nucleation during film formation; then, the current saturates to $\approx 10\ \mu A$. Impressively, after applying V-hold at 2.6 V in the presence of TU, an insoluble black film appears on the Cu foam, and the amount of material deposited correlates with the duration of the V-hold period, confirming that the black film is a byproduct of TU oxidation (Figure S1, Supporting Information). During V-hold at 2.3 and 2.9 V (Figure S2, Supporting Information), lower and higher anodic current flows compared to that of V-hold at 2.6 V, which is consistent with the LSV curves shown in Figure 2a.

To investigate the electrochemical redox behavior of the as-formed layer, CV measurements were conducted using the electrodes after applying V-hold with TU and without TU (Figure 2d). Although the same electrolyte was used (1 M LiTFSI in DOL/DME + 2 wt% $LiNO_3$, without TU), the two electrodes show apparently different redox behaviors. Cu electrode after V-hold without TU exhibits typical ether-based electrolyte reduction peaks at $\approx 1.8$, 1.3, and 0.6 V, which are assigned to the reduction of $LiNO_3$, LiTFSI and DME, respectively,[21,45] and shows negligible oxidation peaks. In contrast, Cu electrode after V-holding with TU shows a large reduction peak at 1.67 V and three oxidation peaks at 1.91, 2.20, and 2.85 V. These redox peaks could be assigned to the conversion reaction of $Cu_2S$, as reported in several studies.[34,46] In addition, redox peaks remain after several CV cycles, further confirming the electrochemical stability of the as-formed layer during continuous cycling (Figure S3, Supporting Information).

For accurate characterization of the film that appeared on the Cu foam during V-hold, X-ray photoelectron spectroscopy (XPS) profiles were obtained after applying V-hold at 2.6 V for 4 h with TU (**Figure 3**a,b). As shown in Figure 3a, signals for $SO_4^{2-}$ (170.7 eV), $SO_3^{2-}$ (167.4 eV), and sulfone (169.4 eV) were detected, which are related to the decomposition of LiTFSI.[36] Notably, signals for $Cu_2S\ 2p_{1/2}$ (163.1 eV) and $Cu_2S\ 2p_{3/2}$ (161.9 eV) appeared after V-hold was applied in the presence of TU.[47,48] Moreover, the relative amount of $Cu_2S$ increased with V-hold time, which can be deduced by comparing the $Cu_2S$ peak area after V-hold was applied for 1 h (Figure S4, Supporting Information) and 4 h. Moreover, the $S_8$ peak (164.7 eV) appeared after V-hold, which supports the aforementioned assumption. The XPS spectra of $Cu_{2p}$ (Figure S5, Supporting Information) and $Cu_{LMM}$ (Figure 3b) further confirm that the assigned peaks in the $S_{2p}$ profiles are mainly $Cu_2S$ rather than Cu metal or CuS; this is inferred from the absence of satellite peaks in the $Cu_{2p}$ XPS spectra and the degree of peak shift in the $Cu_{LMM}$ XPS spectra (Cu–Cu = 568.5 eV, Cu–S = 569.5 eV).[47,48] In contrast, when V-hold was applied at 2.6 V for 4 h without TU in the electrolyte, no signal for $Cu_2S$ and S appeared, confirming that $Cu_2S$ formation occurs due to the oxidation reaction of TU (Figure S6, Supporting Information). For further characterization of $Cu_xSCF$, the Raman spectra of CF and $Cu_xSCF$ were also collected (Figure 3c). As shown in the graph, CF shows negligible peaks,

and Cu does not show a specific Raman peak in that region. In contrast, $Cu_xSCF$ shows several peaks, including ones at 404 and 471 $cm^{-1}$, which are the peaks for $a-Cu_xS$ and $Cu_2S$, verifying the formation of $Cu_2S$ and S species on $Cu_xSCF$.[49] Moreover, peaks appear at 283, 330, and 621 $cm^{-1}$ for $Cu_xSCF$, indicating the formation of CuO,[50] which is ascribed to the oxidation reaction of Cu.

To better understand the SEI structure of $Cu_xSCF$ during Li cycling, XPS depth profiles of Li, S, and Cu of $Cu_xSCF$ after the SEI formation cycle were obtained (Figure 3d–f). As shown in Figure 3d (outer SEI film of $Cu_xSCF$), $Cu_2S$ and $S_8$ on the $Cu_xSCF$ were converted into $Li_2S$ (160.4 eV)/$Li_2S_2$ (161.7 eV)[36,51] and polysulfides (163.2 and 164.4 eV)[52] during the formation cycles. In addition, the amount of $Li_2SO_3$ on the $Cu_xSCF$ increased compared to that on the CF after the formation of the SEI layer (Figure S7, Supporting Information), which was due to the electrochemical reaction of $Li_2S/Li_2S_2$ with the $LiNO_3$ additive.[53,54] Impressively, the $Cu_2S$ signal appeared after etching for 600 s, and its relative amount increased as the etching time increased to 1200 s (Figure 3e,f). Thus, it can be inferred that $Cu_xSCF$ acted as a "lithiophilic" CC due to the $Cu_2S$ that remained beneath the surface film even after the conversion reaction. As shown in the atomic percentage shown in depth profile, Li and S components tend to decrease and Cu components tend to increase toward the inner layer, which is mainly attributed to the abundance of $Cu_2S$ and metallic Cu near the Cu foam (Figure S8 and S9, Supporting Information). Moreover, the decomposition product of LiTFSI (sulfone, $SO_4^{2-}$, $SO_3^{2-}$) is the major S component in the case of 0 s etching; however, its relative ratio decreased, and $Cu_2S/Li_2S/Li_2S_2$ became the major component in the inner layer (Figure 3d–f). This result is consistent with the $Li_{1s}$ XPS depth profile, which shows abundant LiF at the surface of the film and an increased $Li_2S$ ratio toward the inner layer (Figure S10, Supporting Information).[55] These results indicate that the SEI on the $Cu_xSCF$ is composed of $LiF/Li_2S$-rich outer SEI film and an inner layer consisting of $Cu_2S$. For further compositional comparison, the $N_{1s}$, $F_{1s}$, and $O_{1s}$ XPS spectra of CF and $Cu_xSCF$ after the formation cycle were also obtained (Figure S11, Supporting Information). From the $N_{1s}$ and $F_{1s}$ spectra, we can conclude that film formation during V-hold did not affect the N and F components, including $Li_3N$ (397.5 eV), $NSO_2^-$ (399.4 eV),[56] $-CF_x$ (688.8 eV), and LiF (684.8 eV).[54] However, a signal for $Li_2O$ (528.4 eV)[57] appeared in the SEI of $Cu_xSCF$, meaning that the anodic film during V-hold might include an oxidized form of Cu, such as CuO. It is generally known that $Li_2S/Li_2S_2$ is a beneficial component for stable Li cycling due to its high ionic conductivity ($\approx 10^{-5}\ S\ cm^{-1}$) and insulating properties, which can improve $Li^+$ transport kinetics and suppress side reactions with electrolytes, respectively. Moreover, $Li_2S$ and $Li_2O$ could suppress Li dendrite formation due to their good mechanical strength (82.6 and 169 GPa).[21,58] Furthermore, a high content of high-valence sulfur species such as $Li_2SO_3$ can improve the uniformity of the SEI and induce homogenous Li deposition.[53]

Transmission electron microscopy (TEM) analysis was further conducted after Li electrodeposition onto the Cu TEM grid (Li@CF and Li@$Cu_xSCF$) (Figure 3g–i and S12, Supporting Information). As shown in low-magnification TEM images,
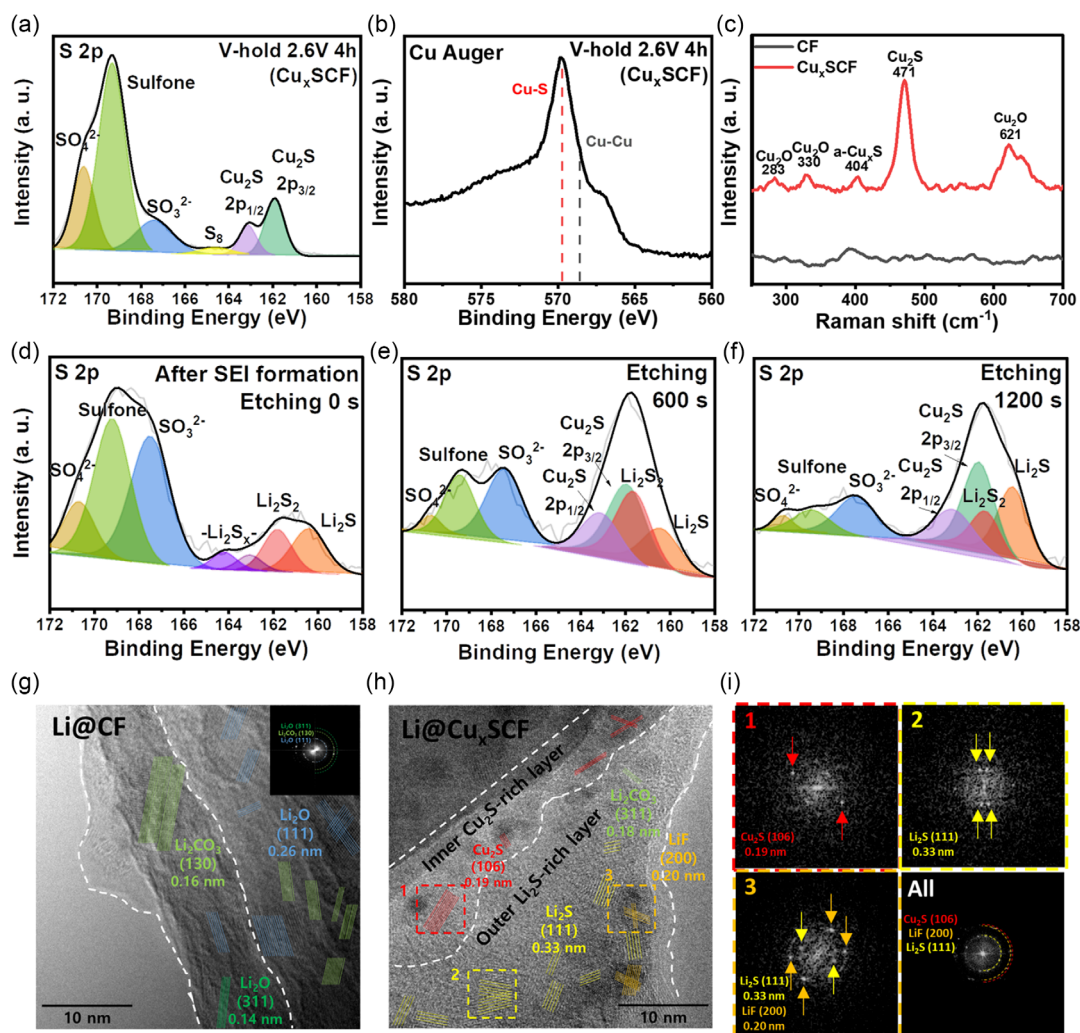
**Figure 3.** a) $S_{2p}$ and b) Cu Auger LMM XPS spectra after applying V-hold at 2.6 V for 4 h with TU ($Cu_xSCF$). c) Raman spectra of bare Cu foam (CF) and $Cu_xSCF$. d–f) $S_{2p}$ XPS depth profiles of $Cu_xSCF$ after the formation cycle. HRTEM images of g) Li@CF and h) Li@$Cu_xSCF$ after Li deposition (0.5 mAh cm$^{-2}$ at a current density of 0.5 mA cm$^{-2}$). i) FFT patterns of selected area shown in (h).

Li@CF and Li@$Cu_xSCF$ showed whisker-like and planar morphology, respectively (Figure S12, Supporting Information). This could be ascribed to the ionically conductive $Li_2S$-rich SEI layer on $Cu_xSCF$, leading to planar growth of Li with suppressed Li dendrite. As shown in high-resolution transmission electron microscopy (HRTEM) images and fast fourier transform (FFT) patterns of Li@CF (Figure 3g), $Li_2CO_3$ (130) (0.16 nm) and $Li_2O$ (311) (0.14 nm) were dominantly found in the outer layer and $Li_2O$ (111) (0.26 nm) was found in the inner layer. In contrast, SEI on Li@$Cu_xSCF$ is composed of $Li_2S$ (111) (0.33 nm) and LiF (200) embedded outer layer, and $Cu_2S$-rich (106) (0.19 nm) inner layer (Figure 3h,i). This result is consistent with the XPS depth profile of $Cu_xSCF$, indicating $Li_2S$-rich outer layer and $Cu_2S$ embedded inner layer (Figure 3d–f).

Meanwhile, subsequent electroplating of Li is also possible in the same electrolyte since the TU additive is compatible with a conventional ether electrolyte. In this manner, we conducted one-pot fabrication of an LMA (Li@$Cu_xSCF$) through an

electrochemical method: 1) surface treatment of CF with $Cu_2S$ layer by applying V-hold and 2) subsequent lithiation by electrodeposition, which is clearly different from other ex situ methods with novel experimental design (Figure S13, Supporting Information). Before V-hold conditions are applied, CF exhibits its original brown color (inset of **Figure 4**) in the absence of a film (CF, Figure 4a). After 4 h of applying V-hold at 2.6 V (denoted as $Cu_xSCF$, inset of Figure 4), CF turned blackish, which was due to the formation of a film derived from the oxidation reaction of TU (Figure 4b) mainly composed of $Cu_2S$ and S (Figure 3a). In contrast, we could not observe any residue on the Cu foam in the scanning electron microscope (SEM) image collected after V-hold without TU; hence, we could confirm that the black film is a byproduct of TU oxidation (Figure S14, Supporting Information). During the following formation cycle, the $Cu_2S$ on $Cu_xSCF$ underwent a conversion reaction (removal of black residue, Figure 4c) at 1.7 V in the initial formation cycle and formed a $Li_2S$-rich SEI layer on the surface. Afterward, Li
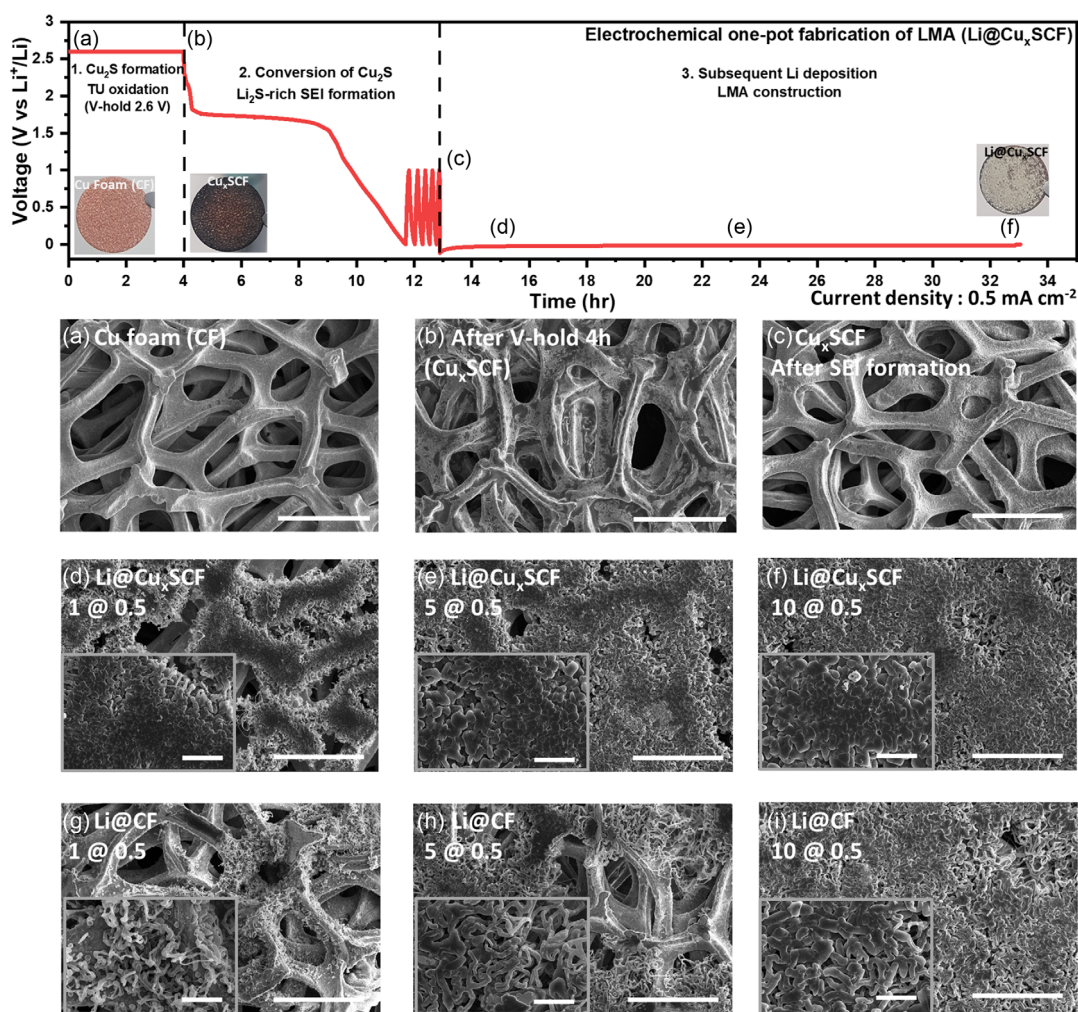
**Figure 4.** Voltage-time curve measured during electrochemical one-pot fabrication of LMA (Li@Cu$_x$SCF, 10@0.5 mA cm$^{-2}$ as an example) (digital images of electrodes shown in graph inset), a–f) SEM images taken during electrochemical one-pot fabrication of Li@Cu$_x$SCF. g–i) Li electrodeposited on a bare CF (Li@CF). Scale bar: 300 μm for low-magnification SEM images, 50 μm for inset images.

deposition occurred sequentially to yield Li@Cu$_x$SCF (Figure 4d–f). The Li deposit on Cu$_x$SCF shows a planar morphology with fewer dendrites on the surface after deposition of 1.0 mAh cm$^{-2}$ (Figure 4d). Even when the capacity of deposited Li increases to 5.0 and 10.0 mAh cm$^{-2}$, the Li deposited on Cu$_x$SCF shows a smooth surface with less dendritic Li formation, confirming the beneficial effects of Cu$_x$SCF in suppressing Li dendrite growth (Figure 4e,f). In contrast, Li grew on CF in dendritic form with severe whiskers and showed inhomogeneous deposition compared to Li@Cu$_x$SCF. As the capacity of deposited Li increases, the compactness of Li also increases in the case of bare CF; however, dendritic forms of Li still exist (Figure 4g–i). The difference in Li morphology is clearly revealed in the high-magnification SEM images of Li@CF and Li@Cu$_x$SCF, showing beneficial effects of Cu$_x$SCF for Li dendrite suppression (Figure S15, Supporting Information). Even at higher current densities (2 and 5 mA cm$^{-2}$), Li@Cu$_x$SCF showed suppressed Li dendrite growth than Li@CF, demonstrating superior Li deposition behavior (Figure S16, Supporting

Information). The improved homogeneity of Li deposits and suppression of Li dendrites in Li@Cu$_x$SCF could be ascribed to the lithiophilic Cu$_2$S layer and Li$_2$S-rich SEI layer of the Cu$_x$SCF substrate.

## 2.1. Electrochemical Performances in LMAs and LMBs

To verify the feasibility of our proposed method for electrochemical surface treatment to yield stable LMAs, the reversibility of Li deposition/stripping on bare CF and Cu$_x$SCF was investigated by measuring CE in a Li/Cu half-cell (**Figure 5**a and S17). First, optimization of the V-hold condition was performed (Figure S17), and we chose 2.6 V for 4 h as the V-hold condition for further LMA fabrication (the details of the optimization are provided in Figure S17). In Figure 5a, Li/Cu$_x$SCF shows a 1.6 times longer cycle life (CF: 130 cycles, Cu$_x$SCF: 220 cycles) and a better average CE of 97.0% compared to 92.9% in Li/CF when measured at 1.0 mA cm$^{-2}$ with a capacity of 1.0 mAh cm$^{-2}$, demonstrating the improved reversibility of Li deposition/stripping upon
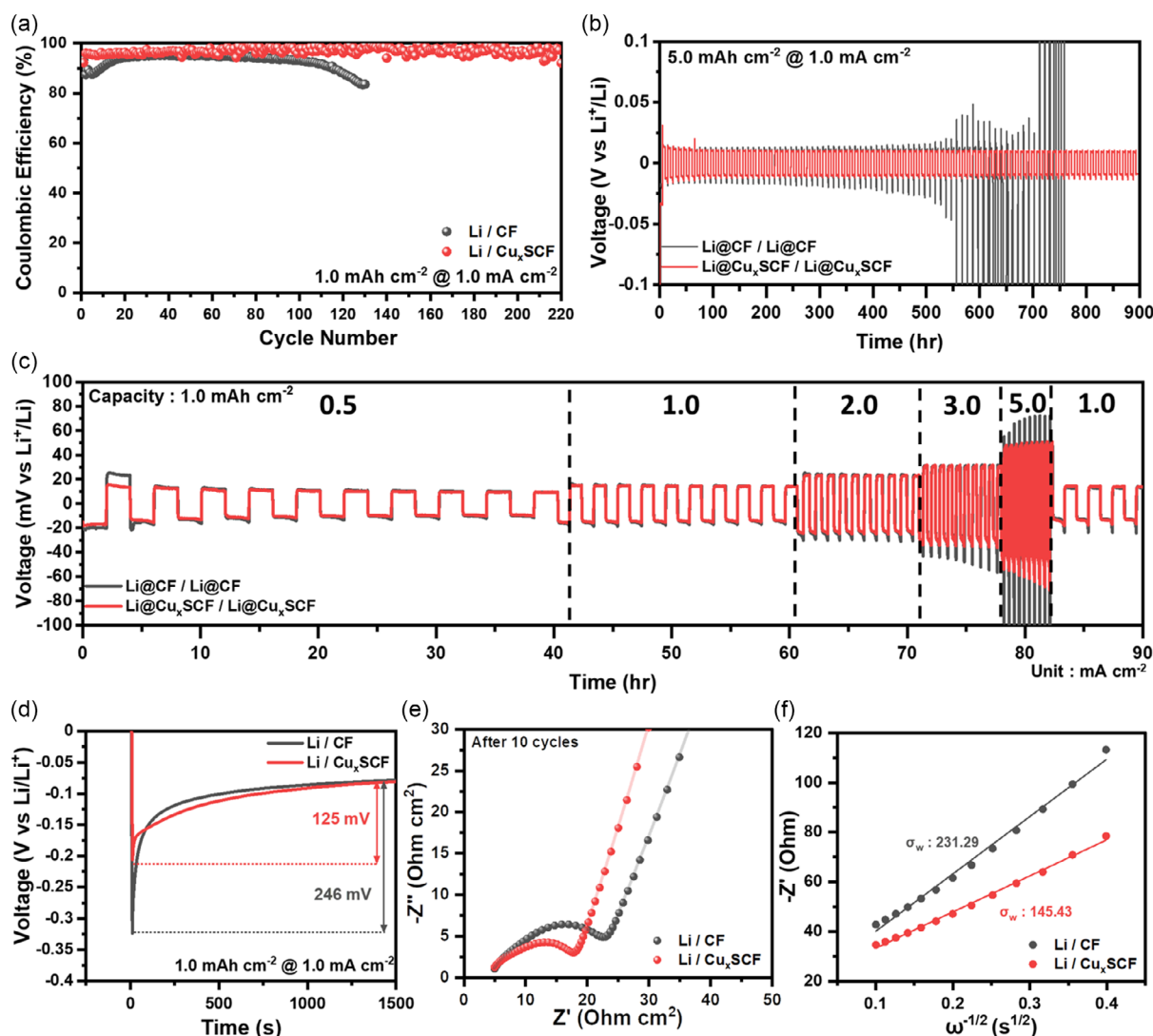
**Figure 5.** a) Coulombic efficiency measured in the Li/Cu cells in Cu foam and $Cu_xSCF$. b) Cyclic performance and c) rate performance of Li@CF and Li@$Cu_x$SCF symmetric cells. d) Voltage profile of the 1st Li deposition on Cu foam and $Cu_x$SCF. e) Nyquist plot of Li/CF and Li/$Cu_x$SCF after the 10th stripping and f) Li@CF/Li@CF and Li@$Cu_x$SCF/Li@$Cu_x$SCF symmetric cells.

surface treatment. Additionally, at a higher current density of 2.0 mA cm$^{-2}$, Li/$Cu_x$SCF also showed better CE than Li/CF, showing its better performance at a high rate (Figure S18). Moreover, Li/$Cu_x$SCF showed smaller polarization than Li/CF during Li cycling, which could be attributed to a reduction in side reactions such as electrolyte consumption and dead Li formation (Figure S19 and S20).

The electrochemical performances of Li@CF and Li@$Cu_x$SCF were also compared by assembling Li@Cu symmetric cells to perform long-term cycling tests (Figure 5b) and rate capability tests (Figure 5c). When cycled at 1.0 mA cm$^{-2}$ with a large capacity of 5.0 mAh cm$^{-2}$, the Li@$Cu_x$SCF symmetrical cell showed stable cycling for 900 h without failure; however, Li@CF exhibited a severe asymmetrical polarization curve after 550 h, which is associated with uncontrolled Li dendrite growth on Li@CF (Figure 5b and S21). Li@$Cu_x$SCF symmetrical cells

also showed enhanced cyclability at different conditions (1.0 mAh cm$^{-2}$ at current densities of 1 and 2 mA cm$^{-2}$) than Li@CF, confirming their superior electrochemical stability (Figure S22). Moreover, the utilization of Li@$Cu_x$SCF in a symmetrical cell resulted in lower polarization than Li@CF, and even at high current densities of 5 mA cm$^{-2}$, the cell maintained symmetrical polarization, demonstrating the superior Li deposition/stripping kinetics and electrochemical stability of Li@$Cu_x$SCF (Figure 5c). Additionally, under ultimately high current densities (from 0.5 to 15 mA cm$^{-2}$, Figure S23), Li@$Cu_x$SCF could maintain lower polarization than Li@CF.

The enhanced electrochemical performance of $Cu_x$SCF compared to bare CF in the Li/Cu cell indicates that our proposed method has considerable effects on the stabilization of Li stripping/deposition behavior, which can be attributed to the presence of the $Cu_2$S layer on $Cu_x$SCF. It is notable that the $Cu_2$S

ADVANCED
SCIENCE NEWS

www.advancedsciencenews.com

small
structures

www.small-structures.com

layer is beneficial for LMA cycling from two aspects: 1) it endows CC with lithiophilicity; and 2) provides a Li$_2$S-rich SEI layer with high ionic conductivity and good mechanical strength. Hence, we further investigated the properties of Cu$_x$SCF with respect to these factors. First, the nucleation overpotential was measured during the 1st deposition of Li at a current density of 1 mA cm$^{-2}$ (Figure 5d) in Li/Cu half cells. The nucleation overpotential is regarded as an energy barrier for the nucleation of metal on a specific substrate, and a low nucleation overpotential is known to indicate enhanced lithiophilicity of the substrate.[59] As shown in the voltage profile, the nucleation overpotential of Cu$_x$SCF is 125 mV, which is lower than that of CF at 246 mV, showing the lithiophilic property of Cu$_x$SCF. This is due to the lithiophilic property of Cu$_2$S on the Cu$_x$SCF substrate, which has good Li$^+$ affinity that is beneficial for the uniform dispersion of Li$^+$ and subsequent uniform Li nucleation. Next, we collected EIS data for the Li/Cu cells after the 10th stripping of Li to compare the film resistance of the SEI layer after activation cycles. Equivalent circuit of Li/Cu cells and fitting results of Nyquist plot is shown in Figure S24 ($R_s$: solution resistance, $R_{cont}$: resistance between CC and coin cell bottom, $R_{SEI}$: resistance of Li$^+$ ion migration in the SEI layer).[60,61] As shown in Figure 5e, Li/Cu$_x$SCF shows a smaller semicircle in the Nyquist plot in the high-frequency region, confirming that the lower SEI resistance in Cu$_x$SCF leads to better Li deposition/stripping behavior with reduced overpotential. This likely occurred because less dead Li is formed and a Li$_2$S-rich SEI layer is present on the Cu$_x$SCF. As shown in the postmortem SEM images, Cu$_x$SCF shows greatly reduced amounts of dead Li compared to bare CF after the 10th stripping in Li/Cu cells due to smoothened Li growth and low dendritic growth (Figure S25 and S26). Even after 50 cycles, Li/Cu$_x$SCF also shows a smaller semicircle compared to Li/CF, further confirming its long-term cycling stability (Figure S27). Additionally, the Li$^+$ diffusion coefficient ($D_{Li^+}$) of the SEI on CF and Cu$_x$SCF was calculated by utilizing the following equation.[62]

$$D_{Li^+} = \frac{R^2 T^2}{2 A^2 n^4 F^4 C^2 \sigma_w^2} \quad (2)$$

In Equation (2), $R$ is the gas constant, $T$ is the absolute temperature, $A$ is the electrode area, $n$ is the number of electrons involved in the reaction, $F$ is Faraday's constant, $C$ is the Li$^+$ concentration in the electrolyte, and $\sigma_w$ is the Warburg coefficient, which can be calculated by fitting a linear curve as shown in the graph and obtaining the slope value (Figure 5f). Note that other than $\sigma_w$, the components are nearly the same for the two electrodes; hence, the relative $D_{Li^+}$ can be calculated by using the following equation.

$$\frac{D_2}{D_1} = \left(\frac{\sigma_1}{\sigma_2}\right)^2 \quad (3)$$

By using Equation (3), it was calculated that the $D_{Li^+}$ of Cu$_x$SCF was ≈2.5 times higher than that of bare CF. The better diffusion coefficient of Li$^+$ and lower resistance of the SEI on Cu$_x$SCF are due to the presence of abundant Li$_2$S/Li$_2$S$_2$/Li$_2$SO$_3$ species in the SEI layer. We further conducted EIS

measurements in a Li@CF symmetrical cell after configuration to investigate the interfacial resistance of the constructed LMAs (Figure S28). Equivalent circuit of Li@Cu symmetric cells and fitting results of Nyquist plot is shown in Figure S29 ($R_s$: solution resistance, $R_{cont}$: resistance between CC and coin cell bottom, $R_{ion}$: migration of Li$^+$ in the pore of Li metal, $R_{SEI}$: resistance of Li$^+$ ion migration in the SEI layer, $R_{ct1}$: charge-transfer resistance of Li$^+$ between Li–SEI and $R_{ct2}$: SEI–electrolyte).[60,61] As shown in the Nyquist plot, smaller resistances for each electrochemical reaction were observed at Li@Cu$_x$SCF compared to Li@CF in symmetrical cells, indicating lower SEI film resistance and more facilitated Li deposition/stripping kinetics in the Li@Cu$_x$SCF anode. In the Tafel curves of Li symmetrical cells (Figure S30), Li@Cu$_x$SCF shows 2.3 times higher exchange current density ($i_0$) of 0.140 mA than Li@CF (0.061 mA). This result shows high charge-transfer rate of Li@Cu$_x$SCF than Li@CF. This could be ascribed to the synergetic effect of the Li$^+$-conducive Li$_2$S-rich SEI layer and lithiophilic CC, which effectively facilitate Li$^+$ transport while homogenizing Li$^+$ flux via lithiophilic sites.

To further verify the feasibility of our proposed LMA fabrication method for practical applications of LMBs, full-cell tests of LFP/Li@Cu cells were performed (**Figure 6**). As shown in Figure 6a, LFP/Li@Cu$_x$SCF could maintain a high capacity retention of 95.6% even after 220 cycles (142.8 mAh g$^{-1}$) and exhibited a high average CE of 99.74% when cycled at 0.5 C (1 C = 170 mA g$^{-1}$) with a low $n/p$ ratio of 1.6. This result is comparable to other reported works, showing feasibility of our work in full cell systems with a low $n/p$ ratio (Figure S31). In contrast, LFP/Li@CF showed rapid capacity losses after only 68 cycles (below 80%, 119.2 mAh g$^{-1}$) and exhibited a low average CE of 99.24%. Moreover, LFP/Li@Cu$_x$SCF showed higher specific capacities of 158.2, 156.0, 148.9, 138.0, 111.8, and 83.0 mAh g$^{-1}$ than LFP/Li@CF (152.8, 150.9, 143.3, 128.3, 89.6, and 53.7 mAh g$^{-1}$) at current densities of 0.1, 0.2, 0.5, 1.0, 2.0, and 3.0 C, respectively (Figure 6b). After the rate capability test, LFP/Li@CF could not recover its specific capacity at 0.5 C, which could be ascribed to the severe deterioration of Li@CF at high current densities. Specifically, when cycled at a high rate of 2.0 C (Figure 6c), LFP/Li@Cu$_x$SCF showed longer cycle life of 425 cycles (capacity retention: 85%, 100.3 mAh g$^{-1}$), which is about three times longer than LFP/Li@CF (147 cycles). As seen from the charge/discharge curves shown in Figure S32–S34, Supporting Information, LFP/Li@Cu$_x$SCF cells showed lower polarization than the LFP/Li@CF cells at various cycling rates. To demonstrate the compatibility of our method in various systems, NCM622/Li@Cu full cells were also tested (Figure 6d). NCM622/Li@Cu$_x$SCF shows higher specific capacities of 149.3, 141.6, 125.5, 107.5, 81.3, and 56.7 mAh g$^{-1}$ compared to LFP/Li@CF (148.6, 136.8, 116.1, 92.7, 61.6, and 38.1 mAh g$^{-1}$) at current densities of 0.1, 0.2, 0.5, 1.0, 2.0, and 3.0 C, respectively. In addition, NCM622/Li@Cu$_x$SCF exhibits a much higher cycling retention of 93.1% (117.1 mAh g$^{-1}$) compared to 62.1% (69.8 mAh g$^{-1}$) for NCM622/Li@CF after 140 cycles and shows smaller polarization than NCM622/Li@CF (Figure S35, Supporting Information). This improved electrochemical performance in NCM622/Li demonstrates the compatibility of our method in ether and ester electrolyte systems. Additionally, NCM811/Li was tested, and
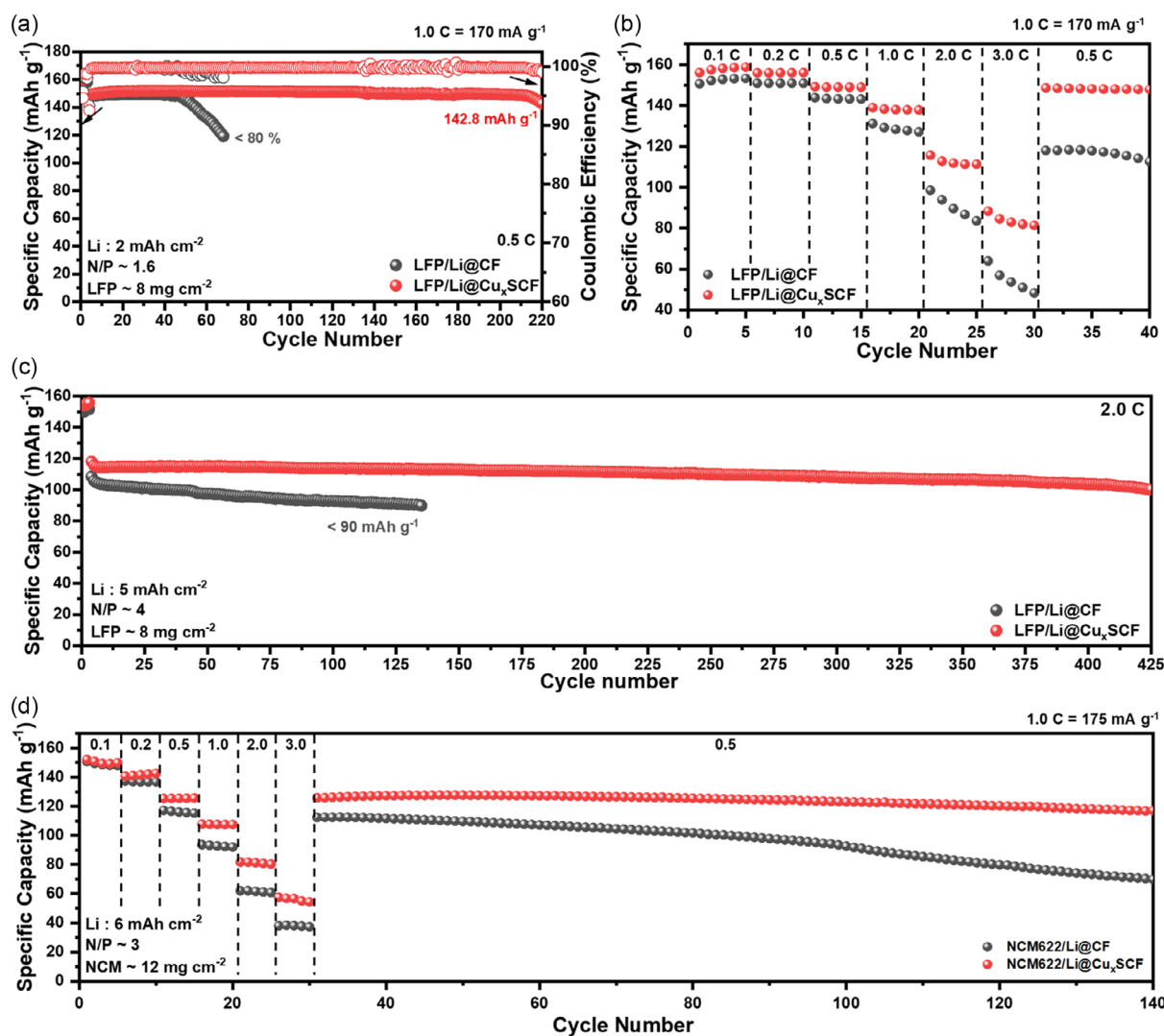
**Figure 6.** a) Cycling performance test at 0.5 C and b) rate capability test of LFP/Li@CF and LFP/Li@Cu$_x$SCF full cells. c) Cycling performance test at 2.0 C in LFP full cells. d) Rate capability test of the NCM622/Li@CF and NCM622/Li@Cu$_x$SCF full cells and further cyclic test.

NCM811/Li@Cu$_x$SCF exhibited enhanced cycling performance and better rate capability than NCM811/Li@CF with lower cell polarization (Figure S36–S39, Supporting Information). This improvement in LMB is ascribed to a better Li deposition/stripping efficiency due to the lithiophilicity of Cu$_2$S and the Li$_2$S-rich SEI layer of Li@Cu$_x$SCF, which improved the electrochemical performance of LMA.

## 3. Conclusions

In summary, we constructed a stable LMA using an electrochemical one-pot fabrication method. By in situ formation of a lithiophilic Cu$_2$S layer through taking a constant potential (V-hold) to oxidize the TU additive followed by Li electrodeposition, LMA with a lithiophilic CC could be obtained by utilizing an electrochemical method and no complex manufacturing processes. TU underwent an oxidation reaction to form an insoluble layer at

2.6 V, which was primarily composed of Cu$_2$S and S. Afterward, the as-formed Cu$_2$S layer underwent a conversion reaction during SEI formation, resulting in nanometrically formed Li$_2$S-rich SEI layer, which had lower film resistance than that of bare CF. As a result, Li@Cu$_x$SCF showed a planar morphology and no severe dendrite formation and showed improved cycling stability and a higher CE in the Li/Cu half cells and Li@Cu symmetrical cells. Notably, LFP/Li@Cu$_x$SCF showed ≈16.5 times lower capacity losses per cycle (0.02%) compared to LFP/Li@CF (0.33%), even at a relatively low $n/p$ ratio of 1.6, and moreover, exhibited an ≈3.2 times longer lifespan (based on 80% retention) when cycled at 0.5 C. Additionally, when cycled at 2.0 C, LFP/Li@Cu$_x$SCF showed capacity retention of 85.0% even after 425 cycles ($n/p = 4$), showing about three times longer cycle life compared to LFP/Li@CF. Moreover, in LMB cells with both types of NCM of Li@Cu$_x$SCF/NCM622 and Li@Cu$_x$SCF/NCM811, greatly enhanced cycling performances were observed.

## Supporting Information

## Acknowledgements

## Conflict of Interest

The authors declare no conflict of interest.

## Data Availability Statement

The data that support the findings of this study are available from the corresponding author upon reasonable request.

## Keywords

[1] X.-B. Cheng, R. Zhang, C.-Z. Zhao, Q. Zhang, *Chem. Rev.* **2017**, *117*, 10403.

[2] D. Lin, Y. Liu, Y. Cui, *Nat. Nanotechnol.* **2017**, *12*, 194.

[3] Y. Jie, X. Ren, R. Cao, W. Cai, S. Jiao, *Adv. Funct. Mater.* **2020**, *30*, 1910777.

[4] K.-Y. Cho, S.-H. Hong, J. Kwon, H. Song, S. Kim, S. Jo, K. Eom, *Appl. Surf. Sci.* **2021**, *554*, 149578.

[5] D. Li, C. Xie, Y. Gao, H. Hu, L. Wang, Z. Zheng, *Adv. Energy Mater.* **2022**, *12*, 2200584.

[6] M. A. Baird, J. Song, R. Tao, R. Ko, B. A. Helms, *ACS Energy Lett.* **2022**, *7*, 3826.

[7] C.-P. Yang, Y.-X. Yin, S.-F. Zhang, N.-W. Li, Y.-G. Guo, *Nat. Commun.* **2015**, *6*, 8058.

[8] H. Qiu, T. Tang, M. Asif, X. Huang, Y. Hou, *Adv. Funct. Mater.* **2019**, *29*, 1808468.

[9] K.-H. Chen, K. N. Wood, E. Kazyak, W. S. LePage, A. L. Davis, A. J. Sanchez, N. P. Dasgupta, *J. Mater. Chem. A* **2017**, *5*, 11671.

[10] J. Steiger, D. Kramer, R. Mönig, *Electrochim. Acta* **2014**, *136*, 529.

[11] X. Chen, B. Zhao, C. Yan, Q. Zhang, *Adv. Mater.* **2021**, *33*, 2004128.

[12] Z. Li, J. Huang, B. Yann Liaw, V. Metzler, J. Zhang, *J. Power Sources* **2014**, *254*, 168.

[13] S. Wang, Y. Chen, Q. Fang, J. Huang, X. Wang, S. Chen, S. Zhang, *Energy Storage Mater.* **2023**, *54*, 596.

[14] Z. Huang, G. Zhou, W. Lv, Y. Deng, Y. Zhang, C. Zhang, F. Kang, Q.-H. Yang, *Nano Energy* **2019**, *61*, 47.

[15] A. J. Louli, A. Eldesoky, R. Weber, M. Genovese, M. Coon, J. deGooyer, Z. Deng, R. T. White, J. Lee, T. Rodgers, R. Petibon, S. Hy, S. J. H. Cheng, J. R. Dahn, *Nat. Energy* **2020**, *5*, 693.

[16] Z. Wu, H. Liu, J. Holoubek, C. Anderson, L. Shi, H. Khemchandani, D. Lu, D. Liu, C. Niu, J. Xiao, P. Liu, *ACS Energy Lett.* **2022**, *7*, 2701.

[17] J. Qian, W. A. Henderson, W. Xu, P. Bhattacharya, M. Engelhard, O. Borodin, J.-G. Zhang, *Nat. Commun.* **2015**, *6*, 6362.

[18] S. Chen, J. Zheng, D. Mei, K. S. Han, M. H. Engelhard, W. Zhao, W. Xu, J. Liu, J.-G. Zhang, *Adv. Mater.* **2018**, *30*, 1706102.

[19] J.-F. Ding, R. Xu, N. Yao, X. Chen, Y. Xiao, Y.-X. Yao, C. Yan, J. Xie, J.-Q. Huang, *Angew. Chem. Int. Ed.* **2021**, *60*, 11442.

[20] Y. Liu, D. Lin, P. Y. Yuen, K. Liu, J. Xie, R. H. Dauskardt, Y. Cui, *Adv. Mater.* **2017**, *29*, 1605531.

[21] C. Zhang, Q. Lan, Y. Liu, J. Wu, H. Shao, H. Zhan, Y. Yang, *Electrochim. Acta* **2019**, *306*, 407.

[22] K. Min Yang, K. Yang, M. Cho, S. Kim, Y. Lee, *Chem. Eng. J.* **2023**, *454*, 140191.

[23] L. Tan, C. Wei, Y. Zhang, Y. An, S. Xiong, J. Feng, *Chem. Eng. J.* **2022**, *442*, 136243.

[24] Y.-K. Lee, K.-Y. Cho, S. Lee, J. Choi, G. Lee, H.-I. Joh, K. Eom, S. Lee, *Adv. Energy Mater.* **2023**, *13*, 2203770.

[25] H. Cheng, C. Gao, N. Cai, M. Wang, *Chem. Commun.* **2021**, *57*, 3708.

[26] K. Huang, S. Song, Y. Xiang, *J. Phys. Conf. Ser.* **2021**, *2009*, 012080.

[27] Y. Ye, Y. Liu, J. Wu, Y. Yang, *J. Power Sources* **2020**, *472*, 228520.

[28] J. Luan, Q. Zhang, H. Yuan, Z. Peng, Y. Tang, S. Wu, H. Wang, *Chem. Eng. J.* **2020**, *395*, 124922.

[29] C. Zhang, W. Lv, G. Zhou, Z. Huang, Y. Zhang, R. Lyu, H. Wu, Q. Yun, F. Kang, Q.-H. Yang, *Adv. Energy Mater.* **2018**, *8*, 1703404.

[30] K. Wang, W. Wang, J. Deng, X. Jiang, G. Xu, H. Gong, N. Zhang, D. Li, *J. Alloys Compd.* **2021**, *889*, 161597.

[31] R. Xu, Y. Zhou, X. Tang, F. Wang, Q. Dong, T. Wang, C. Tong, C. Li, Z. Wei, *Small* **2023**, *19*, 2205709.

[32] Y. Fan, X. He, H. Li, Y. Huang, C. Sun, H. Liu, E. Huangzhang, F. Sun, X. Zhao, J. Nan, *Chem. Eng. J.* **2022**, *450*, 138384.

[33] Z. Huang, C. Zhang, W. Lv, G. Zhou, Y. Zhang, Y. Deng, H. Wu, F. Kang, Q.-H. Yang, *J. Mater. Chem. A* **2019**, *7*, 727.

[34] Z. Yang, W. Liu, Q. Chen, X. Wang, W. Zhang, Q. Zhang, J. Zuo, Y. Yao, X. Gu, K. Si, K. Liu, J. Wang, Y. Gong, *Adv. Mater.* **2023**, *35*, 2210130.

[35] Q. Lan, Y. Liu, J. Qin, X. Meng, Y. Zhao, T. Xu, H. Zhan, *Electrochim. Acta* **2023**, *437*, 141490.

[36] W. Li, H. Yao, K. Yan, G. Zheng, Z. Liang, Y.-M. Chiang, Y. Cui, *Nat. Commun.* **2015**, *6*, 7436.

[37] Y. Roh, Y.-J. Kim, J. Lee, J. Baek, J.-H. Lee, J. K. Yoon, H. J. Hah, J. Y. Kim, H.-T. Kim, *ACS Appl. Energy Mater.* **2020**, *3*, 10070.

[38] R. Li, Y. Fan, C. Zhao, A. Hu, B. Zhou, M. He, J. Chen, Z. Yan, Y. Pan, J. Long, *Small Methods* **2023**, *7*, 2201177.

[39] Y. Zhang, W. Lv, Z. Huang, G. Zhou, Y. Deng, J. Zhang, C. Zhang, B. Hao, Q. Qi, Y.-B. He, F. Kang, Q.-H. Yang, *Sci. Bull.* **2019**, *64*, 910.

[40] J. Zhao, G. Zhou, K. Yan, J. Xie, Y. Li, L. Liao, Y. Jin, K. Liu, P.-C. Hsu, J. Wang, H.-M. Cheng, Y. Cui, *Nat. Nanotechnol.* **2017**, *12*, 993.

[41] A. E. Bolzán, A. S. M. A. Haseeb, P. L. Schilardi, R. C. V. Piatti, R. C. Salvarezza, A. J. Arvia, *J. Electroanal. Chem.* **2001**, *500*, 533.

[42] A. S. M. A. Haseeb, P. L. Schilardi, A. E. Bolzan, R. C. V. Piatti, R. C. Salvarezza, A. J. Arvia, *J. Electroanal. Chem.* **2001**, *500*, 543.

[43] Q. Wang, C. Yang, J. Yang, K. Wu, C. Hu, J. Lu, W. Liu, X. Sun, J. Qiu, H. Zhou, *Adv. Mater.* **2019**, *31*, 1903248.

[44] S. Kim, K.-Y. Cho, J. Kwon, K. Sim, D. Seok, H. Tak, J. Jo, K. Eom, *Small* **2023**, *19*, 2207222.

[45] C. Jiang, Q. Jia, M. Tang, K. Fan, Y. Chen, M. Sun, S. Xu, Y. Wu, C. Zhang, J. Ma, C. Wang, W. Hu, *Angew. Chem. Int. Ed.* **2021**, *60*, 10871.

[46] Y. Fu, A. Manthiram, *Electrochim. Acta* **2013**, *109*, 716.

[47] A. Ghahremaninezhad, E. Asselin, D. G. Dixon, *J. Phys. Chem. C* **2011**, *115*, 9320.

[48] A. Tang, S. Qu, K. Li, Y. Hou, F. Teng, J. Cao, Y. Wang, Z. Wang, *Nanotechnology* **2010**, *21*, 285602.

[49] Y. Havryliuk, M. Y. Valakh, V. Dzhagan, O. Greshchuk, V. Yukhymchuk, A. Raevskaya, O. Stroyuk, O. Selyshchev, N. Gaponik, D. R. T. Zahn, *RSC Adv.* **2018**, *8*, 30736.

[50] G. Durai, P. Kuppusami, K. Viswanathan, *J. Mater. Sci. Mater. Electron.* **2018**, *29*, 2051.

[51] G. Li, Q. Huang, X. He, Y. Gao, D. Wang, S. H. Kim, D. Wang, *ACS Nano* **2018**, *12*, 1500.

[52] S.-H. Moon, J.-H. Kim, J.-H. Shin, J.-S. Jang, S.-B. Kim, S.-N. Lee, S.-H. Kwon, K.-W. Park, *J. Alloys Compd.* **2022**, *904*, 164120.

[53] L.-P. Hou, L.-Y. Yao, C.-X. Bi, J. Xie, B.-Q. Li, J.-Q. Huang, X.-Q. Zhang, *J. Energy Chem.* **2022**, *68*, 300.

[54] D. Aurbach, E. Pollak, R. Elazari, G. Salitra, C. S. Kelley, J. Affinito, *J. Electrochem. Soc.* **2009**, *156*, A694.

[55] H. Zhang, C. Shen, Y. Huang, Z. Liu, *Appl. Surf. Sci.* **2021**, *537*, 147983.

[56] H. M. Bintang, S. Lee, S. Shin, B. G. Kim, H.-G. Jung, D. Whang, H.-D. Lim, *Chem. Eng. J.* **2021**, *424*, 130524.

[57] V. Winkler, G. Kilibarda, S. Schlabach, D. V. Szabó, T. Hanemann, M. Bruns, *J. Phys. Chem. C* **2016**, *120*, 24706.

[58] G. Wan, F. Guo, H. Li, Y. Cao, X. Ai, J. Qian, Y. Li, H. Yang, *ACS Appl. Mater. Interfaces* **2018**, *10*, 593.

[59] K. Yan, Z. Lu, H.-W. Lee, F. Xiong, P.-C. Hsu, Y. Li, J. Zhao, S. Chu, Y. Cui, *Nat. Energy* **2016**, *1*, 16010.

[60] M. Srout, M. Carboni, J.-A. Gonzalez, S. Trabesinger, *Small* **2023**, *19*, 2206252.

[61] S. Drvarič Talian, J. Bobnar, A. R. Sinigoj, I. Humar, M. Gaberšček, *J. Phys. Chem. C* **2019**, *123*, 27997.

[62] Z. Li, Q. He, C. Zhou, Y. Li, Z. Liu, X. Hong, X. Xu, Y. Zhao, L. Mai, *Energy Storage Mater.* **2021**, *37*, 40.